Coastal Engineering 156 (2020) 103622

Contents lists available at ScienceDirect

Coastal Engineering

journal homepage: http://www.elsevier.com/locate/coastaleng

Unstructured finite element mesh decimation for real-time Hurricane storm surge forecasting

Matthew V. Bilskie [a,*], Scott C. Hagen [a,b,c], Stephen C. Medeiros [d]

[a] Louisiana State University, Center for Coastal Resiliency, 124B Sea Grant Hall, Baton Rouge, LA, 70803, USA
[b] Louisiana State University, Department of Civil and Environmental Engineering, USA
[c] Louisiana State University, Center for Computation and Technology, USA
[d] Embry-Riddle Aeronautical University, Department of Civil Engineering, 1 Aerospace Blvd, Daytona Beach, FL, 32114, USA

ARTICLE INFO

Keywords:
Storm surge
Unstructured mesh
Mesh decimation
Coastal flooding

ABSTRACT

A previously developed research-grade (e.g. high-resolution) unstructured mesh of the northern Gulf of Mexico (named NGOM3) is optimized to produce a computationally efficient forecast-grade mesh for deployment in a real-time hurricane storm surge early warning system. The real-time mesh is developed from a mesh decimation scheme with focus on the coastal floodplain. The mesh decimation scheme reduces mesh nodes and elements from the research-grade mesh while preserving the representation of the bare-earth topography. The resulting real-time unstructured mesh (named NGOM-RT) contains 64% less mesh nodes than the research-grade mesh. Comparison of (ADCIRC + SWAN) simulated times-series and peak water levels to observations between the research-grade and real-time-grade meshes for Hurricanes Ivan (2004), Dennis (2005), Katrina (2005), and Isaac (2012) show virtually no difference. Model simulations with the NGOM-RT mesh are 1.5–2.0 times faster than using NGOM3 on the same number of compute cores.

1. Introduction

The northern Gulf of Mexico (NGOM) experiences frequent hurricanes that can generate large storm surges resulting in coastal floods and are among the costliest and deadliest natural disasters (Ashley and Ashley, 2008). This region has been affected by numerous recent storms such as Hurricanes Ivan (2004), Dennis (2005), Katrina (2005), Rita (2005), Gustav (2008), Ike (2008), Isaac (2012), Hermine (2016), Harvey (2017), Irma (2017), Nate (2017), and Michael (2018). Accurate forecasting of peak water levels and overland inundation is useful in order to prepare for such events, mitigate property damage, and limit loss of life (Munroe et al., 2018; Wolshon et al., 2005). Numerical computer models can be used to predict the flood location, timing, magnitude, and duration. Such predictions are used by a variety of local, regional and federal institutions in order to design evacuation strategies, activate floodgates and surge barriers, and aid in post-disaster recovery operations.

In the past decade, physics-based numerical models that compute water levels and velocities for astronomic tides and tropical cyclone-driven storm surges have improved, particularly with the development of new data collection technology (e.g. lidar) and readily available high-performance computational resources. With these enhanced technologies, the focus has been on developing models with finer spatial and temporal resolution. Finer resolution allows for enhanced representation of the landscape, specifically topography, bathymetry, raised features, and vegetation (Bilskie et al., 2015; Bilskie and Hagen, 2013; Cobell et al., 2013; Hope et al., 2013; Medeiros et al., 2015). In addition, advancements have been made in improving the physics via tight-coupling of wind-wave models to storm surge models (Bunya et al., 2010; Dietrich et al., 2011a, 2011b, 2012, 2013; Funakoshi et al., 2008) and improved tropical cyclone wind drag formulations (Black et al., 2007; Powell et al., 2003; Powell, 2006; Dietrich et al., 2011a). Such advancements have increased model accuracy of hurricane-driven water levels and related overland inundation across coastal floodplains.

Numerical hurricane storm surge models are now deployed in real-time and results are being adopted by emergency managers and stakeholders in their decision-making framework (Morrow and Lazo, 2014; Burston et al., 2015). Even with the advancements and availability of computational power, applying physics-based storm surge models that are highly descriptive of topographic and bathymetric features in real-time is a challenge. First and foremost, the storm surge simulation for a particular forecast must be performed (and results disseminated to

* Corresponding author.
E-mail address: mbilsk3@lsu.edu (M.V. Bilskie).

https://doi.org/10.1016/j.coastaleng.2019.103622
Received 15 July 2019; Received in revised form 21 October 2019; Accepted 10 December 2019
Available online 19 December 2019
0378-3839/© 2019 Elsevier B.V. All rights reserved.

end-users) faster than actual time - in most cases the simulation must be performed in a fraction of actual time (total simulation time on the order of 1–2 h). Second, the total number of available computational cores for a given high performance computer (HPC) is likely to be limited. In addition, the size of the model domain and level of resolution must be large and fine enough, respectively, to cover a wide-range of possible hurricanes (Dietrich et al., 2012). Therefore, a balance must be achieved in the level of model detail (i.e. resolution and region of interest) and simulation turnaround time. This leads to the question of how to discretize a model domain with sufficient detail so that it can run in a reasonable time frame and produce storm surge results that can be specifically used by emergency managers in near real-time.

Many studies have developed methods to semi-automate the mesh generation and others have aimed at strategically placing computational points within the model domain to minimize model error (Gorman et al., 2008; Bilgili et al., 2006; Danilov, 2013). For example, Hagen et al. (2001) developed mesh size functions based on *a posteriori* results from an astronomic tide simulation using localized truncation error analysis (LTEA). They found that LTEA created a superior unstructured mesh for astronomic tide modeling than wavelength to mesh size-based meshing criteria (Westerink et al., 1994). These methods have been expanded to include non-linear terms of the shallow water equations and have been successfully implemented for large and complex domains (Hagen et al., 2002, 2006; Parrish and Hagen, 2007, 2009; Bacopoulos et al., 2011). Recent techniques in automated mesh generation for shallow water flow models have been developed to consider minimal inputs (shoreline and elevation data) to generate a quality unstructured mesh using signed distance functions and force-balance algorithms to guide mesh sizing criteria (Persson and Strang, 2004; Conroy et al., 2012; Roberts et al., 2018).

The methods mentioned above have been proven to work well in coastal waters (where a depth of water is consistently maintained), but little work has been performed to create quality and computational efficient unstructured meshes across the coastal floodplain (normally dry areas) that become inundated at high tide or during storm surge events. Coastal floodplains are complex landscapes that contain sharp gradients in elevation and a variety of natural and urbanized landscape features (Medeiros et al., 2012; Bilskie and Hagen, 2013). Furthermore, the process of an advancing or receding flood wave is a modeling challenge (Medeiros and Hagen, 2012). Typical methods of mesh generation across the landscape attempt to resolve significant terrain features (e.g. levees, floodwalls, ridges, bayous) that can inhibit or conduct flows (Bilskie et al., 2015; Coggin et al., 2011). Such methods are useful in developing more topographically accurate meshes, but do little to guide the mesh generation process in terms of local mesh sizing. Therefore, mesh resolution is determined from the mesh creator's intuition and experience selecting a minimum element size to achieve a selected minimum time step along with the computational resources available. This procedure often results in over-resolved meshes because the spatial variability of terrain is not included in the mesh generation process (Bilskie et al., 2015).

The goal of this study is to develop a detailed unstructured finite element mesh with specific focus on the Mississippi, Alabama, and Florida panhandle coastal floodplain for use in a real-time storm surge modeling framework. To achieve this goal we adopt a mesh decimation technique to relax local mesh element sizes while preserving the geometric accuracy of the coastal floodplain as represented by the mesh and its solution of the shallow water equations. This ultimately leads to a mesh that can be run efficiently and therefore employed in the real-time storm surge forecasting framework.

The paper is organized in the following manner. The hydrodynamic model is described as well as the algorithms employed to adjust local element sizes, including mesh decimation. The results of these techniques are presented along with simulation results, including validation, for Hurricanes Ivan (2004), Dennis (2005), Katrina (2005), and Isaac (2012). In addition, the compute time for simulations employing the research-grade vs. real-time unstructured meshes are shown. The paper concludes with a summary and future research.

2. Methods

2.1. ADCIRC + SWAN model

The tightly coupled advanced circulation (ADCIRC) and simulating waves nearshore (SWAN) models were used to simulate hurricane-driven coastal circulation and overland inundation. ADCIRC solves for water surface elevations and depth-averaged velocities across an unstructured finite element mesh using a modified form of the shallow water equations, specifically the generalized wave continuity equation and depth-averaged momentum equations (Kinnmark; Kolar et al., 1994; Luettich and Westerink, 2004; Westerink et al., 2008). In this study, the ADCIRC time-step is 1.0 s to satisfy the Courant number criteria and the implicit solver was used. Surface roughness parameters are based on the Coastal Change Analysis Program (C-CAP) land use land cover (LULC) (http://www.csc.noaa.gov/) (Dietrich et al., 2011a; Bilskie et al., 2015). Hydraulic bottom friction was parameterized via spatially-varying Manning's n coefficients and vegetation canopy was parameterized by surface directional roughness lengths (Atkinson et al., 2011) and a canopy coefficient that limits the winds ability to transfer momentum to the water surface in dense canopies (Westerink et al., 2008). Offshore Manning's n values were assigned based on the bottom sediment type (Buczkowski et al., 2006) and local depth (Bilskie et al., 2016a; Kennedy et al., 2011; Martyr et al., 2013).

SWAN is a phase-averaged wave model that solves the action balance equation for relative frequency and wave direction, which evolves in geographical space, spectral space, and time across an unstructured finite element mesh (Booij et al., 1999; Dietrich et al., 2011b; Ris et al., 1999; Zijlema, 2010). Simulated wave frequencies were discretized logarithmically into 40 frequency bins ranging from 0.31384 to 1.420416 Hz and directions into 36 10° bins. Wind inputs and wind-induced wave growth were based on Cavaleri and Rizzoli (1981) and Komen et al. (1984) with modified whitecapping updated by Rogers et al. (2003). Bottom roughness was converted from Manning's n to roughness lengths (Dietrich et al., 2011a; Madsen et al., 1988). Depth-induced wave breaking was equal to 0.73 based on Battjes and Janssen (1978). A spectral propagation velocity limiter was included to limit false wave refraction in regions with coarse mesh resolution away from the study area (Dietrich et al., 2013).

The ADCIRC + SWAN model are tightly-coupled and operate on the same unstructured finite element mesh. ADCIRC passes water levels and depth-averaged currents to SWAN. SWAN then computes wave radiation stress gradients that are passed to ADCIRC. This occurs every 600 s, which is also the SWAN time step.

2.2. Unstructured finite element mesh development

The development of the real-time unstructured mesh (named NGOM-RT, RT for real-time) begins with the high-resolution, research-grade, NGOM3 unstructured finite element mesh (Bilskie et al., 2016a). We refer to NGOM3 as a "research-grade" mesh because it is the culmination of more than a decade of our efforts to provide the most detailed description of the northern Gulf to-date (Bilskie et al., 2014, 2015, 2016a, 2016b; Bilskie and Hagen, 2013; Coggin et al., 2011; Hagen and Parrish, 2004; Hagen, 2001; Passeri et al., 2015a, 2015b, 2016; Salisbury et al., 2011). The NGOM3 mesh consists of 5.5 million nodes and spans the western north Atlantic Ocean (from the 60° west Meridian), Caribbean Sea, and Gulf of Mexico with focus on the Mississippi, Alabama, and Florida panhandle coastal floodplain up to the 15 m elevation contour. It was developed to provide the most complete description of tide and surge dynamics in this region with nominal concern for computational cost. With its highly descriptive properties and extensive validation it serves as a benchmark of comparison for any subsequent

efforts.

The NGOM3 computational mesh serves as a starting point to create a real-time mesh via the reduction of mesh elements. This was accomplished through the five steps, described in detail in the following sections and outlined in Fig. 1.

1. Mesh nodes and elements in the nearshore portion (e.g. sounds, estuary, bays, and rivers) of the study domain were extracted from the NGOM3 mesh.
2. Mesh nodes were reduced in the open ocean through localized truncation error analysis (LTEA).
3. The upland model domain was trimmed to remove regions of high topography that are unlikely to become inundated from a tropical cyclone.
4. A mesh decimation algorithm was employed to determine regions where the mesh can be coarsened while still preserving the terrain.
5. Vertical feature lines were extracted.
6. An advancing front paving algorithm was employed to generate an unstructured mesh of the coastal floodplain based on the vertical features and mesh size function.
7. Elevations from a high-resolution digital elevation model (DEM) were interpolated to the mesh nodes.

2.2.1. Nearshore and inland waterways

The research-grade NGOM3 mesh includes high-resolution along the shoreline (20–100 m element size) in the nearshore areas of Mississippi, Alabama, and the Florida panhandle. The resolution and mesh topology for this area will be preserved. Mesh resolution in the nearshore is constrained by the width of the smallest water body features that must be included in the model. For this work, water-body features (inlets, rivers, and Intracoastal Waterway) that have a width greater than 100 m are included so at least three elements with spacing of 20–40 m can span their respective width. This is to ensure that, at a minimum, these bathymetric features are represented by the mesh as a trapezoidal cross-section. Away from the water-body features, the nearshore area was defined as the 3 m (NAVD88) depth contour in Mississippi and Alabama and out to the 20 m (NAVD88) depth contour along the Florida panhandle.

2.2.2. Localized truncation error analysis

The unstructured finite element mesh for water-only regions spanning the western north Atlantic (WNAT) model domain (western north Atlantic, Caribbean Sea, and Gulf of Mexico) was generated using localized truncation analysis with complex derivatives (LTEA + CD) (Parrish and Hagen, 2009). The goal of LTEA + CD is to evenly distribute local truncation errors across the entire model domain by relaxing the mesh resolution in areas where truncation errors are low (Bacopoulos et al., 2011; Hagen et al., 2000, 2002, 2006; Hagen, 2001; Parrish and Hagen, 2009). The result of LTEA + CD is a spatially varying elemental size function. A mesh paving algorithm is then used to create the unstructured finite element mesh by using the LTEA + CD-generated node spacing requirements (Hagen et al., 2006). The LTEA + CD localized truncation error of linear Galerkin finite elements is:

$$\widehat{\tau}^{+}_{ME} = \frac{\Delta^6}{1440}\underbrace{\left[\omega(i\widehat{v}_0 - \widehat{u}_0) + (\tau\widehat{v})_0 + i(\tau\widehat{u})_0 - i(f\widehat{v})_0 + (f\widehat{u})_0\right]}_{\text{derivative term}}{}^{6} \tag{1}$$

where Δ is the distance from the central node to that of any of its neighbors, ω is tide constituent frequency, $\widehat{u}$ and $\widehat{v}$ are the complex velocities in the x- and y-direction, respectively, τ is the bottom stress, and f is Coriolis force (Bacopoulos et al., 2011). Target local element sizes obtained from Equation (1) are rearranged into the form of $\Delta^* = aD$, where a is an arbitrary scale factor and D is a deterministic scale factor. A uniform scale factor was used to indirectly limit the gradient in the target element size and D was applied based on a Gaussian distribution to smooth the gradient in target element sizes (Parrish and Hagen, 2007; Bacopoulos et al., 2011). A maximum element size gradient of 0.75 was used, which limits adjacent elements to being no larger than a factor of 2 in elemental area (big/small).

We begin with an arbitrary and generally spatially uniform high-resolution mesh (Fig. 3A) of the WNAT model domain with bathymetric elevations derived from SRTM_30 (Becker et al., 2009). The mesh contains 456,000 nodes and 900,000 elements with local element sizes ranging from 300 m to 25 km. The mesh was included in a fully non-linear 90-day ADCIRC simulation (5.0 s time step), including advection, Coriolis force, and quadratic bottom friction. The model was forced with seven tidal constituents along the open ocean boundary (K1, O1, M2, S2, N2, K2, and Q1). Water levels and depth-averaged currents

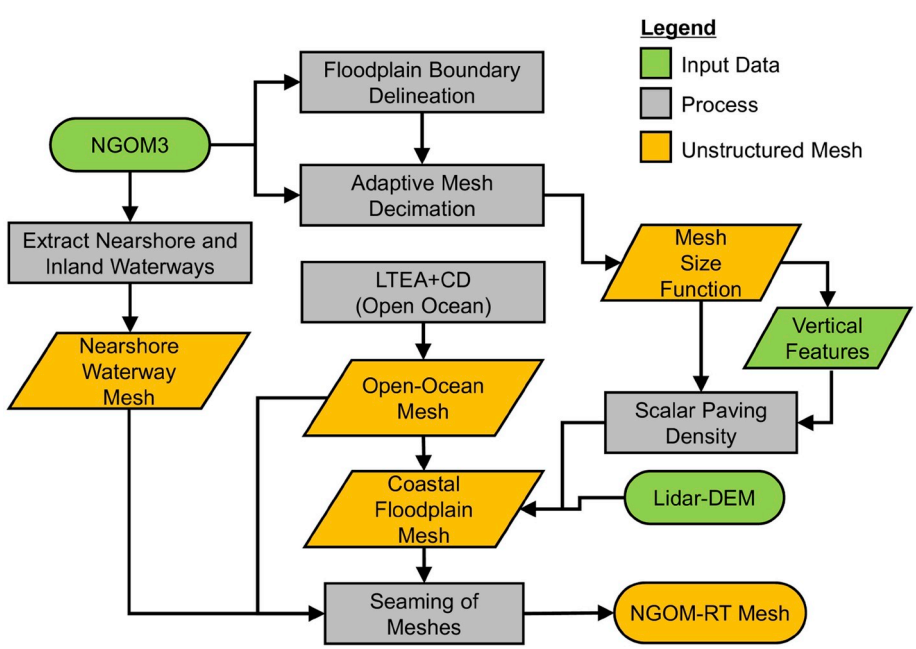

Fig. 1. Flowchart outlining the unstructured mesh generation process that stems from the high-resolution NGOM3 and previously developed lidar-derived DEM and vertical features (Bilskie and Hagen, 2013; Bilskie et al., 2015).

were resynthesized from the last 45 days of simulation and used as inputs into LTEA + CD. Target element sizes were computed for 23 individual tidal constituents at each mesh node and the minimum value was selected to generate the final target element size for the WNAT model domain. This process was repeated for a second iteration, with the input mesh being the output mesh of the first iteration.

2.2.3. Floodplain boundary delineation

The NGOM3 model includes normally dry regions up to the 15 m elevation contour across Mississippi, Alabama, and the Florida panhandle. The high upland elevation contour was necessary as the NGOM3 model was used to study the dynamics of coastal flooding under future sea level rise scenarios. Since a 15 m storm tide is unlikely in this region under present-day conditions, portions of the upper floodplain were removed from the mesh to reduce the number of computational points. A maximum of maximums (MOM) water level surface was derived from NGOM3 ADCIRC + SWAN simulations forced by 219 synthetic storms computed from Bilskie et al. (2019). The final upload boundary is the extent of the MOM boundary plus a 500 m buffer. The boundary generally follows the 10–15 m elevation contour in Mississippi and Alabama and the 5 m elevation contour along the Florida panhandle.

2.2.4. Adaptive mesh decimation

Mesh decimation provides a means to coarsen mesh node density in certain regions of the domain. This can be accomplished through input geometry, solution gradients, visual appearance, and error functions. Edge collapse is one common mesh decimation algorithm. The edge collapse algorithm considers a target element edge between two mesh nodes, relocates each mesh node to the same location, connects the incident edges to one of the mesh nodes, removes the other mesh node, and removes mesh elements that have disjoint nodes (Fig. 2) (Garland and Heckbert, 1997; Jia et al. 2006).

In this work, mesh decimation is applied to the overland regions of the NGOM3 unstructured finite element mesh. Recall that the mesh represents a large set of bare-earth elevations for given latitudes and longitudes. The goal is to approximate the terrain represented by the denser mesh with a lower resolution mesh by removing nodes that do not increase the approximation error above a given threshold (Coll et al., 2011). Typically, nodes can be removed until either 1) a set number of mesh elements or nodes are achieved, 2) a global error threshold is met or 3) a combination of 1 and 2.

We employed Matlab's *reducepatch* algorithm for mesh decimation. The input was the unstructured mesh of the NGOM3 coastal floodplain from Mississippi to Florida's Big Bend region (containing 3,002,723 mesh elements). A mesh element threshold of 450,000 was used to reduce the total number of mesh elements by 85%. The value of 450,000 was obtained based on an iterative process through visual inspection of the decimated mesh's representation of the topography. Matlab's *reducepatch* algorithm was selected because of its ease of use of use to perform mesh decimation as well as its speed. Unfortunately, detailed information regarding the *reducepatch* function is not publicly available. A drawback of implementing the *reducepatch* mesh decimation is that mesh quality is not preserved. Therefore, a spatially varying mesh size function was based only on the decimated mesh (Fig. 1).

2.2.5. Vertical features

Vertical features are defined as linear raised or sunken bare-earth terrain features that can impact the path, pattern, and magnitude of flooding. Vertical features are typically long and narrow with respect to the desired local element size and are substantially higher in elevation than the surrounding terrain. Examples of vertical features include raised railroads and roadbeds, flood walls, levees, and natural ridges. Because the width (w) of these features are narrow compared to the local element size ($w_{vf} << \Delta$) their width scales cannot be adequately represented by the unstructured mesh without drastically decreasing the local element size. Therefore, vertical features require special treatment during the mesh generation process.

This work takes advantage of the vertical features previously developed by Bilskie et al. (2015). A short summary is provided, but for algorithm details, parameters, and psuedo-code please refer to Bilskie et al. (2015). Vertical features were semi-automatically generated and based on the delineation of small watersheds from a bare earth-lidar-derived DEM. The watershed lines and DEM were then examined to relate the watershed line elevations with respect to the surrounding terrain. Vertical features were extracted from the watershed line if they met certain metrics with respect to length, height, and width. The extracted vertical features were then compared to the mesh size function generated from the decimated mesh. Final cleaning of the extracted feature lines involved removing lines that are shorter and too close together compared to the local element size.

2.2.6. Coastal floodplain mesh generation - scalar paving density

An unstructured mesh of the coastal floodplain was generated using an advancing front paving algorithm (George et al., 1991; George and Seveno, 1994) within the Surface Water Modeling System (SMS) (Aquaveo, 2014). The inputs to the paving algorithm include 1) a polygon of the model domain (exterior constraints), 2) vertical feature lines (interior constraints), and 3) mesh size function. The paving algorithm attempts to create mesh elements similar in size to those prescribed by the size function while also preserving mesh quality. In addition, elements were inserted so their edges align with vertical feature lines where present. The paving process was performed for 43 sub-domains that make up the desired coastal floodplain portion of the model domain. Finally, the LTEA-drived mesh for the open ocean and waterways was seamed with the mesh of the coastal floodplain and inland waterways.

2.2.7. Bathymetry and topography

A seamless digital elevation model (DEM) for the nearshore and coastal floodplain regions was generated from the latest and best-available bathymetric and topographic data (Bilskie et al., 2016a). Bathymetric data included National Ocean Service (NOS) hydrographic surveys (http://www.ngdc.noaa.gov/mgg/bathymetry/hydro.html),

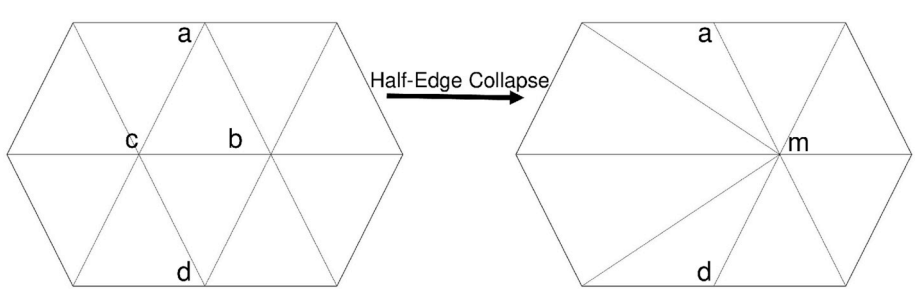

Fig. 2. Example of half-edge collapse. Mesh node c is removed and becomes mesh node m and incident edges (a-c and d-c) are removed. Then disjoint node c is removed.

US Army Corps of Engineers submerged channel surveys and river cross sections and boat-mounted depth sounder surveys. Elevation data were obtained from recent airborne bare-earth lidar provided by the Northwest Florida Water Management District, NOAA Digital Coast, Coastal Topographic Lidar (http://coast.noaa.gov/digitalcoast), NASA Experimental Advanced Airborne Research Lidar (EAARL) system, and Joint Airborne Lidar Bathymetry Technical Center of Expertise (JALBTCX) CHARTS system. All elevations not referenced to NAVD88 were converted to NAVD88 using NOAA's VDatum (https://vdatum.noaa.gov/). Additional details on the development of the seamless DEM can be found in Bilskie et al. (2016a) and Bilskie et al. (2015), and Bilskie and Hagen (2013).

The seamless DEM was interpolated to the unstructured mesh using the cell area averaging method of Bilskie and Hagen (2013), but with a 2x smoothing criteria (https://github.com/mattbilskie/DEM2GRD). Smoothing was done to ensure that the mesh represented the coastal landscape while relaxing steep elevation gradients across a single element. The shallow-water equations are not intended to resolve large flow gradients (i.e. turbulence) and their presence can lead to numerical instabilities.

2.2.8. Additional mesh modifications

Alongside the development of the NGOM3 mesh, flood protection infrastructure (e.g. levees and floodwalls) across the Louisiana coast has also been meshed (Bunya et al., 2010). Although the scope of the current modeling study does not focus on Louisiana, areas of southeastern Louisiana (east of the Mississippi River levee) are included in the unstructured mesh. These areas are included to allow surge to propagate and attenuate across the floodplain rather than including a no-flow boundary condition at the shoreline. The ADCIRC mesh developed for the 2012 Louisiana Coastal Master Plan was used for regions east of the Mississippi River (CPRA, 2017), including the model description of the flood protection infrastructure. In addition, the NGOM-RT includes a wave radiation boundary condition to include flows in the Mississippi River.

2.3. Model forcing

The NGOM3 and NGOM-RT models were forced by astronomic tides along the open ocean boundary located at the 60° west meridian (K1, O1, M2, S2, N2, K2, and Q1) as derived from the Oregon State TPXO7.2 tidal atlas (Egbert et al., 1994; Egbert and Erofeeva, 2002). Due to the large model domain tidal potential was also included for the same tidal constituents. Each simulation began as a cold-start and the astronomic tides were ramped up by a hyperbolic function over the course of 7 days, followed by an addition 7 days of dynamic steady state (tide spin-up). The NGOM-RT model was also forced with a constant river flow of 4 730 cubic meters per second to represent average conditions during the hurricane season for the Mississippi River at Baton Rouge.

The storm surge simulations were hot-started from the tide spin-up simulation. Wind and pressure fields were developed using a blend of modeled winds and objectively analyzed measurements as outlined by Bunya et al. (2010) and Bilskie et al. (2016a). Ivan, Dennis, and Katrina were based on NOAA's H*WIND (Hurricane Research Division Wind Analysis System) (Powell et al., 1998) for the core of the storm and then blended with Gulf-scale winds from the IOKA (Interactive Objective Kinematic Analysis) system (Cox et al. 1995 Swail). The core of Hurricane Isaac was modeled by the latest version of the TC96 mesoscale model (Thompson and Cardone, 1996). Thirty minute sustained marine-based winds at 10 m height were applied to the ADCIRC simulation every 15 min. To include wind reduction due to above ground obstacles the ADCIRC model used directional wind reductions (every 30°) derived from NOAA CCAP land use land cover data (Bilskie et al., 2016a).

2.4. Measurements and evaluation of model performance

Measurements include observations of time-series water levels and high water marks (HWM). Time-series water levels for each hurricane event were obtained from NOAA tide gages, US Army Corps of Engineers (USACE) water level stations, and USGS gages. Prior to Hurricane Isaac the USGS deployed over 60 temporary gages around the predicted impact zone. Most of the gages were placed on normally dry land. In addition to time-series water levels, model results were compared to measured HWMs obtained from the Federal Emergency Management Agency (FEMA) and NOAA. A list of all observation stations and data source agencies can be found in Table 1.

For each hurricane event model performance is evaluated by comparing simulated results to measured data using scatter index (SI):

$$SI = \frac{\sqrt{\frac{1}{N}\sum_{i=1}^{N}(E_i - \overline{E})^2}}{\frac{1}{N}\sum_{i=1}^{N}|O_i|} \tag{2}$$

and bias:

$$bias = \frac{\frac{1}{N}\sum_{i=1}^{N}E_i}{\frac{1}{N}\sum_{i=1}^{N}|O_i|} \tag{3}$$

where N is the number of measurements, $E_i = S_i - O_i$, S is the simulated water level, and O is the observed water level (Hope et al., 2013). Water level stations that had erroneous data, influence of rainfall runoff, or lacked a defined peak were omitted.

Observed HWM were assessed and measurements that contained error, included wave runup, river discharges, or rainfall runoff effects were discarded (Luther et al., 2007). Additionally, HWMs that contained simulated errors outside the interquartile range (IQR) were removed from the analysis:

$$E_i < Q_1 + 1.5 * IQR \tag{4}$$

$$E_i > Q_3 + 1.5 * IQR \tag{5}$$

where Q_1 and Q_3 are the first and third quartiles and $IQR = Q_3 - Q_1$. The error at each HWM is $E_i = S_i - O_i$. The method of using IQR for the removal of HWMs is common among storm surge validation studies (Bunya et al., 2010; Dietrich et al., 2011a; Bilskie et al., 2016a).

In addition, simulated peak water levels between each model were quantified using root mean square (RMS) difference at the mesh nodes:

$$RMS = \sqrt{\frac{1}{N}\sum_{i=1}^{N}(\eta_F - \eta_C)^2} \tag{6}$$

where η_F and η_C are the simulated peak water levels from the fine (NGOM3) and coarse (NGOM-RT) mesh solutions.

3. Results

3.1. Localized truncation error analysis

The local element size of the initial high-resolution mesh of the WNAT is compared to the first and second iteration of the LTEA-derived meshes (Fig. 3). In general, mesh resolution is coarsened in the deeper waters of the Gulf of Mexico, Caribbean Sea, and western Atlantic and high resolution exists at regions of large bathymetric gradients (e.g. the continental shelf and Bahamas Bank), shallow depths, and the shoreline. Approximately 25% of the model domain includes element spacing less than 10 km for both LTEA-derived meshes in contrast to 86% of the initial mesh (Fig. 4). This indicates that much of the total area of the model domain is over-resolved in the initial mesh for a real-time storm surge application. Specifically, the deep waters are over-resolved and hydrodynamically important geophysical features such as the

Table 1
Summary of NGOM-RT water level statistics for recorded water level measurements. SI and bias were only computed for time-series data. Statistics and errors for peak storm surge were only computed if the data set had 10 reliable stations.

Storm	Data Source	No. of stations			ADCIRC to measured HWMs					Measured HWMs		Estimated ADCIRC errors	
			SI (m)	**Bias**	**No. of HWMs**	**Slope**	R^2	**Avg. Abs. Diff. (m)**	**Std. Dev. (m)**	**Avg. Abs. Diff. (m)**	**Std. Dev. (m)**	**Avg. Abs. Diff. (m)**	**Std. Dev. (m)**
Ivan	NOAA	3	0.213	0.143									
	USACE	8	0.302	0.076									
	FEMA				124	0.87	0.52	0.461	0.527	0.135	0.228	0.311	0.446
	All	11	0.278	0.094	124	0.87	0.52	0.461	0.527	0.135	0.228	0.311	0.446
Dennis	NOAA/ NDBC	14	0.242	−0.036	14	0.99	0.98	0.060	0.063	0.058	0.080	0.002	0.000
	FEMA				146	0.91	0.71	0.246	0.263	0.041	0.080	0.205	0.250
	All	14	0.242	−0.036	158	0.92	0.78	0.224	0.241	0.044	0.078	0.180	0.228
Katrina	NOAA	9	0.248	−0.003									
	USACE	15	0.186	0.001	12	1.02	0.96	0.105	0.146	0.000	0.000	0.105	0.146
	USGS	6	0.230	−0.060									
	FEMA				314	0.99	0.96	0.298	0.372	0.104	0.201	0.195	0.313
	All	30	0.213	−0.012	326	0.99	0.96	0.291	0.366	0.105	0.202	0.187	0.306
Isaac	NOAA	15	0.188	−0.039	16	1.00	0.94	0.071	0.085	0.000	0.000	0.071	0.085
	USGS Perm.	13	0.251	−0.147	12	0.99	0.88	0.191	0.246	0.000	0.000	0.191	0.246
	USGS SSS	53	0.168	−0.071	42	1.01	0.88	0.124	0.105	0.000	0.000	0.124	0.105
	USGS Rapid	7	0.167	−0.102									
	NOAA HWM				42	0.98	0.70	0.286	0.337	0.067	0.129	0.219	0.311
	All	88	0.184	−0.079	112	0.98	0.88	0.177	0.215	0.042	0.087	0.136	0.197

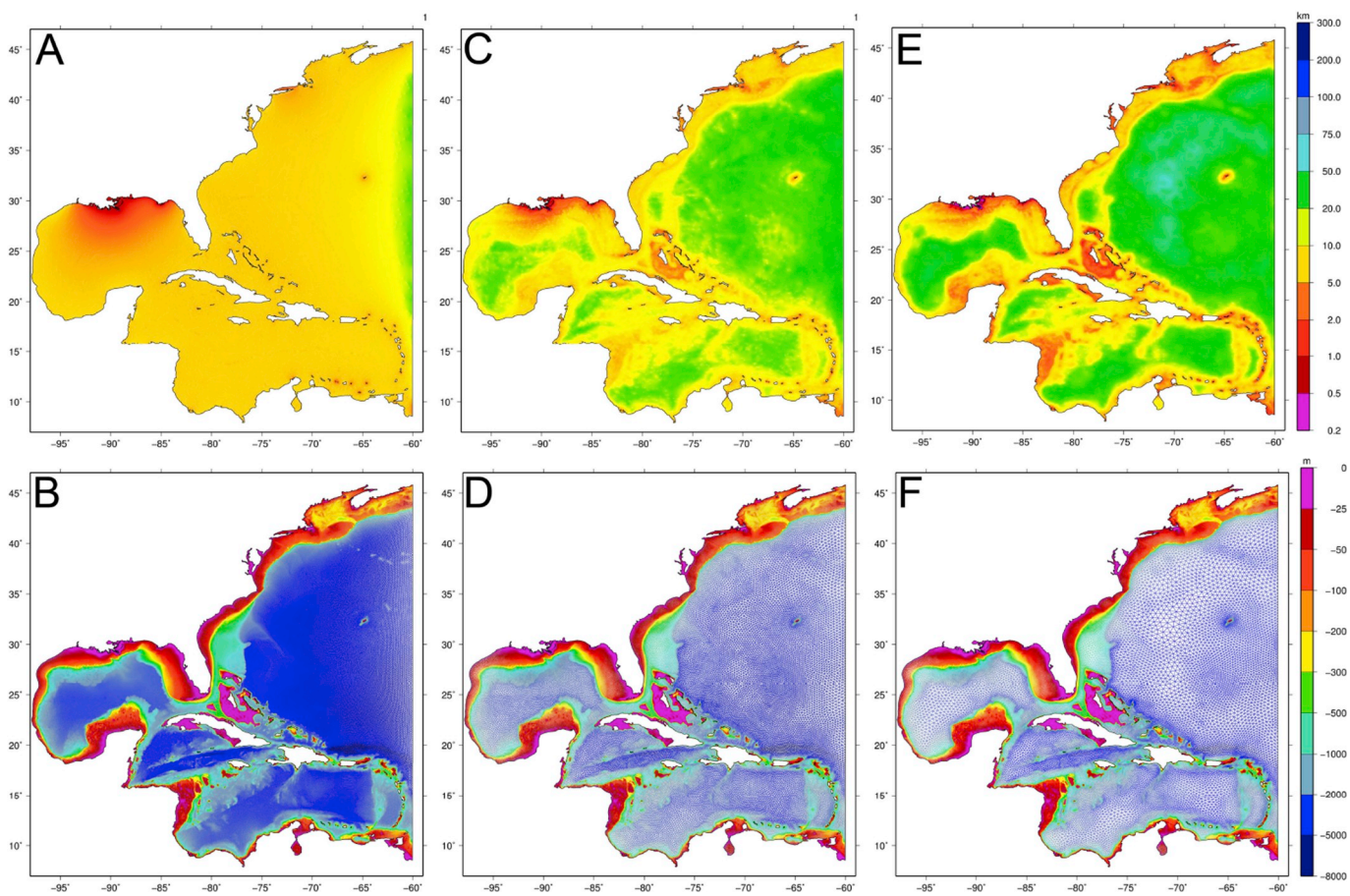

Fig. 3. A) Local element size (km) and B) and bathymetry (m) for the initial mesh to be used for LTEA (457k nodes). C) Local element size resulting from the first iteration of LTEA (215k nodes) and the D) resulting mesh and bathymetric representation. E) Local element size for the mesh obtained from the second iteration of LTEA (596k nodes) and the F) resulting mesh and bathymetric representation.

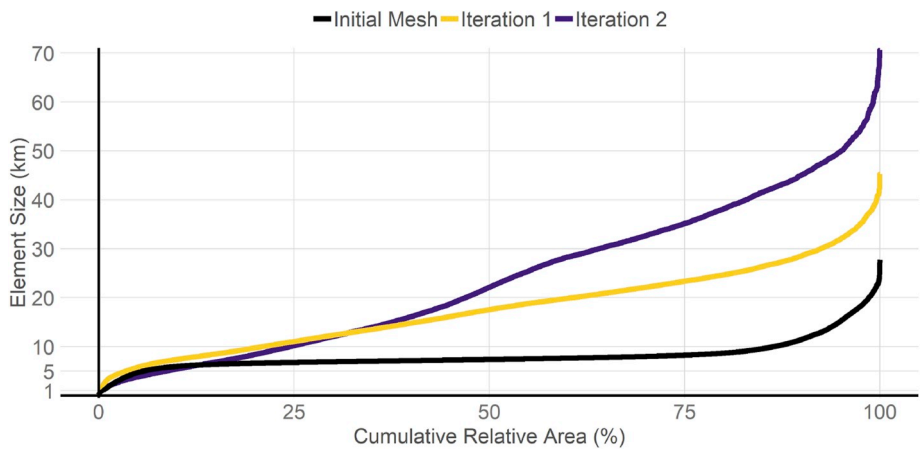

Fig. 4. The local element size (km) related to the cumulative relative area (%) that encompasses the western North Atlantic model domain.

continental shelf (specifically along the U.S. east coast) are under-resolved.

The first iteration of LTEA + CD results in spatially varying element sizes ranging from 0.1 to 45 km and a total node count of 215,231. Areas along the northern Gulf of Mexico include the highest resolution on the order of 1 km followed by the Bahamas Bank at 4–5 km resolution (Fig. 3C–D). Element spacing is generally around 7–9 km on the continental shelf and rapidly increases to 15 km and greater towards deeper water.

The second and final iteration of LTEA + CD yields a range of element sizes from 0.1 to 70 km with a total node count of 595,921 (Fig. 4E–F). High resolution is retained along the northern Gulf of Mexico coast; however, element spacing across the Bahamas Bank and on the continental shelf varies as compared to the first iteration. In

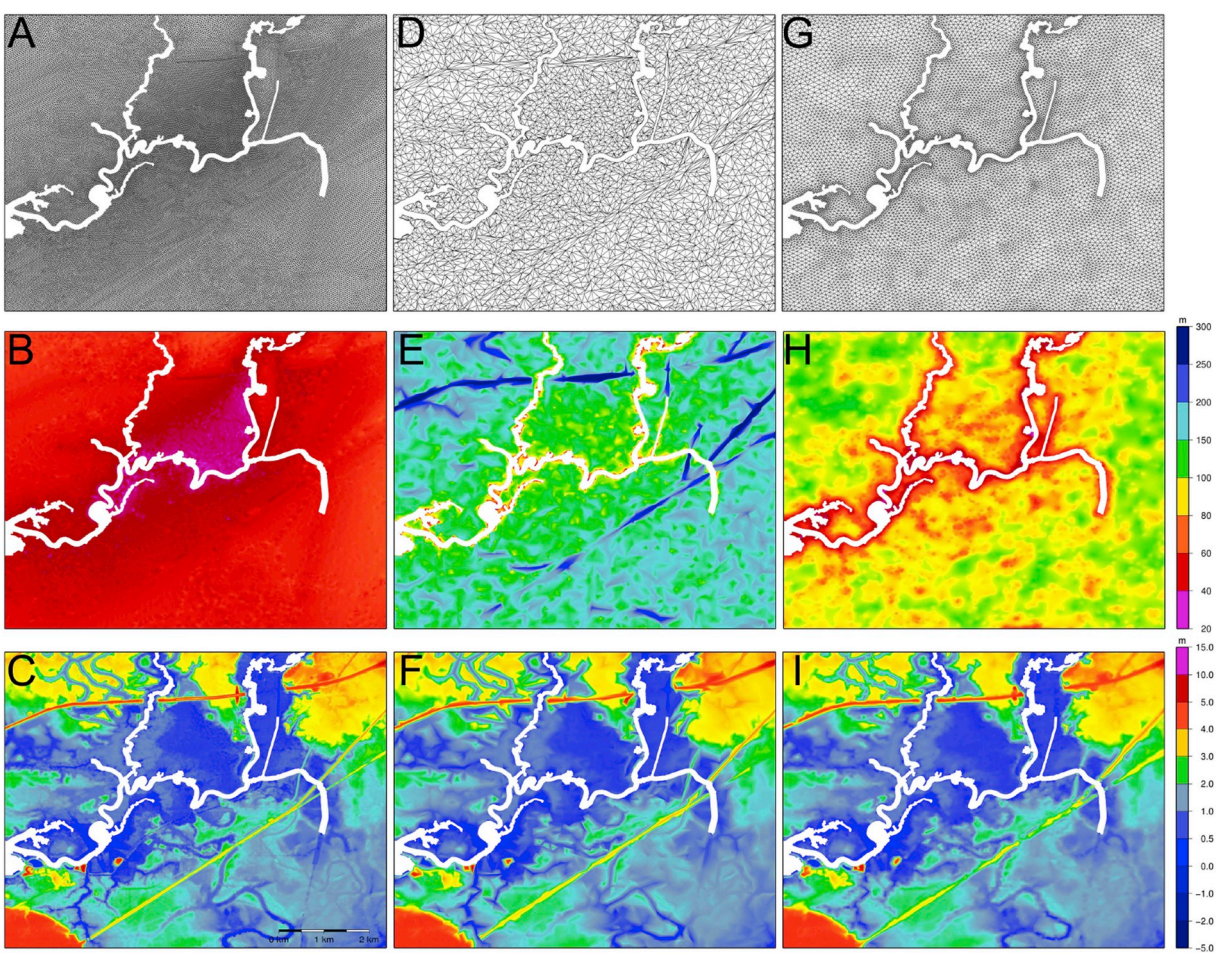

Fig. 5. Unstructured finite element mesh across the floodplain near Pascagoula, MS as represented by the A) research-grade mesh (43,336 nodes and 84,756 elements as shown), D) decimated mesh (4 746 nodes and 8 128 elements as shown), and G) real-time-grade mesh (11,976 nodes and 22,051 elements as shown). Local element size (m) and topography (m, NAVD88) as represented by the B–C) research-grade mesh, E-F) decimated mesh, and H–I) real-time-grade mesh, respectively. Water bodies have been removed for visualization and analysis purposes.

addition, mesh resolution rapidly reduces to greater than 30 km from the continental shelf to the deep ocean and by as much as 70 km in the Atlantic (west of Bermuda).

3.2. Adaptive mesh decimation and scalar paving density

Mesh decimation across the coastal floodplain, using the high-resolution NGOM3 model as the input, results in fewer nodes and elements. For the full floodplain region of interest, the original mesh included 1,561,493 nodes and 3,002,723 elements and the decimated mesh reduced the count to 276,569 nodes and 450,000 elements for a node and element count reduction of 82% and 85%, respectively (recall the constraints set on the mesh decimation were to reduce the total element count by 85%). Fig. 5 shows an example of the mesh decimation procedure for a region in Pascagoula, MS (adjacent to the Escatawpa River). The original high-resolution mesh of this area contains local element sizes of 50 m (Fig. 5A–B) and describes the overland topography with high detail (Fig. 5C). Vertical features in this region include Interstate 10 (spanning east-west to north) and U.S. 90 (spanning southwest-northeast). The decimated mesh (Fig. 5D) yields a coarser node density and larger elements ranging from 100 to 300 m (Fig. 5E). The description of the topography is retained with the decimated mesh, specifically the vertical features (Fig. 5F). However, visual inspection indicates that mesh quality is compromised (Fig. 5D).

The result of scalar paving density using the local element spacing from the decimated mesh (Fig. 5E) and vertical feature lines is a mesh with similar resolution as the decimated mesh, but with enhanced element quality (Fig. 5G). The final coastal floodplain mesh contains 557,886 nodes and 1,017,487 elements, which is a 64% reduction in total node count. For the area shown in Fig. 5H, the resolution ranges from 40 to 150 m, with most of the area containing resolution of 80–100 m. The benefits of employing an unstructured finite element mesh are now better utilized in the new mesh with the additional benefit of retaining topographic accuracy when compared to the original source mesh (Fig. 5I).

The final mesh (coined NGOM-RT), after seaming the new coastal floodplain mesh with the inland waterways and LTEA-derived offshore mesh, includes 2,051,346 nodes and 4,065,583 elements (Figs. 6–7). The NGOM-RT has an overall nodal reduction of 62.7% compared to the high-resolution NGOM3 mesh. A reduction of 64% in node count spanned element sizes of less than 100 m, a 53% reduction in nodes sizes between 100 and 200 m, and a 62% reduction in nodes of element sizes ranging from 200 to 500 m (Fig. 8). In addition to coarsening mesh elements in regions of high node density, such as across the coastal floodplain, mesh node density is coarsened in areas of open water. The final mesh reduced nodes counts by 77% in element sizes from 1 to 10 km (Fig. 8). Element sizes greater than 10 km now span 75% of the entire model domain in contrast to the 45% of the original NGOM3 mesh (Fig. 9).

3.3. Model validation

Hurricanes Ivan, Dennis, Katrina, and Isaac were selected for model validation as they made landfall along the NGOM coast and contain a plethora of measured data. In addition, Bilskie et al. (2016a) performed a synoptic analysis and detailed validation with an earlier version of the NGOM3 model for all four hurricanes focused on the Mississippi, Alabama, and Florida panhandle.

The NGOM3 and NGOM-RT simulated water levels and waves agree with measurements along the Mississippi, Alabama, and Florida panhandle for Hurricanes Ivan, Dennis, Katrina, and Isaac (Table 1, Fig. 10 and Supplementary S1–S8). SI and bias of time-series water levels ranged from 0.18 to 0.28 to −0.08–0.09 m across the range of storms for the NGOM-RT model simulation, respectively, indicating the simulated time-series water levels agree with the measurements. Simulated peak water levels match measured HWMs (including gage peaks) with estimated peak water level errors ranging from 0.14 to 0.31 m. Combining all HWMs and gage peak errors across the four storms yields a coefficient of determination (R^2) of 0.96 for both models and a slope of the linear regression line of 0.95 and 0.98 for the NGOM3 and NGOM-RT models, respectively.

3.4. NGOM3 and NGOM-RT intercomparison

Table 2 shows difference among the error statistics between the NGOM3 and NGOM-RT model results. Similar to the minor differences in the HWM errors (Fig. 10) there is virtually no difference in the error statistics. Differences in SI and bias are less than 10 cm. The differences between the model's errors (with respect to the average absolute difference) range from −0.04 - 0.02 m. These results can be considered negligible. Larger differences in model errors are found for Hurricanes Katrina and Isaac, albeit they are still minor. These storms made landfall along the Louisiana/Mississippi border and differences are a result of the addition of flood protection infrastructure in southeastern Louisiana in the NGOM-RT mesh.

To this point, simulated water levels have been compared to measurements and errors were similar among the NGOM3 and NGOM-RT models. To compare simulated water levels between the NGOM3 and NGOM-RT models across the full coastal floodplain RMS differences (Eq. (6)) were calculated for mesh nodes shallower than 10 m (Dietrich et al., 2018) (including normally dry areas) in the region surrounding the landfall location. For comparison purposes, the NGOM-RT results were linearly interpolated to the NGOM3 mesh. The RMS difference in simulated peaks was 0.11 m, 0.10 m, 0.18 m, and 0.55 m for Hurricanes Ivan, Dennis, Katrina, and Isaac, respectively. The RMS differences are larger for Katrina and Isaac because these storms impacted western

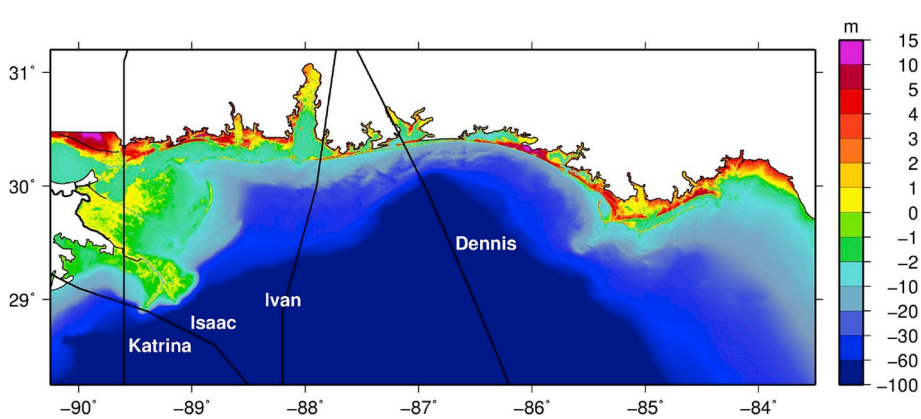

Fig. 6. Topography and bathymetry are represented by the NGOM-RT unstructured finite element mesh (m, NAVD88). Hurricane tracks are shown as the black lines.

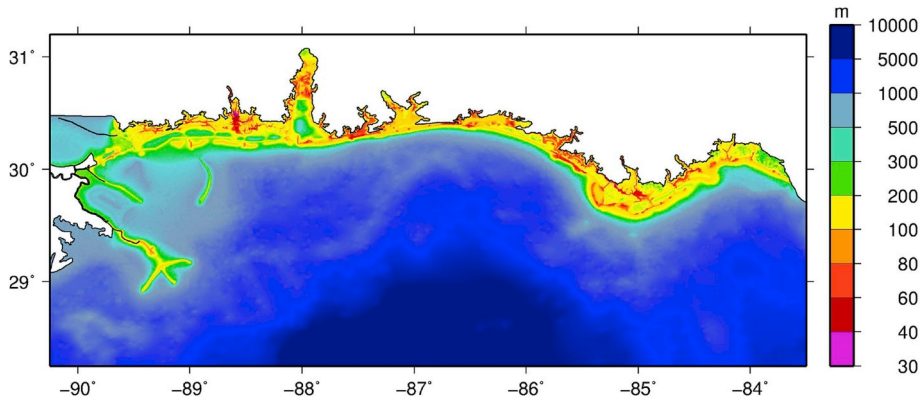

Fig. 7. Local element size (m) of the NGOM-RT unstructured finte element mesh.

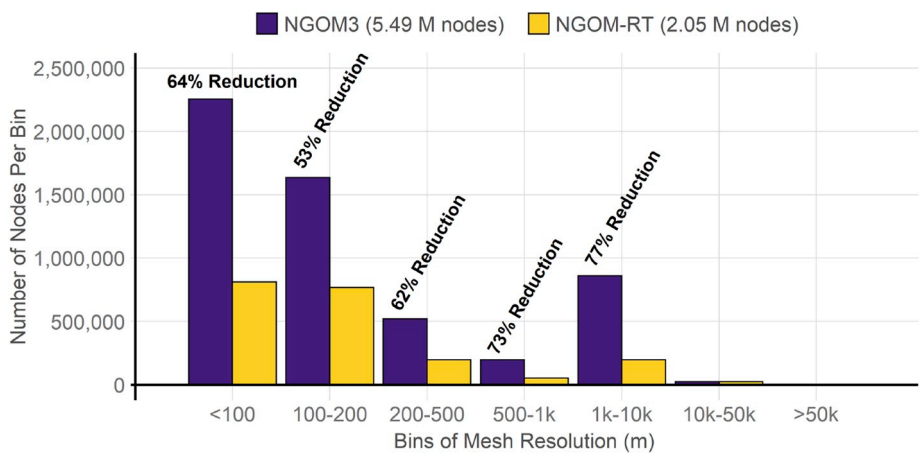

Fig. 8. Bins of mesh resolution for the original NGOM3 and final mesh (NGOM-RT).

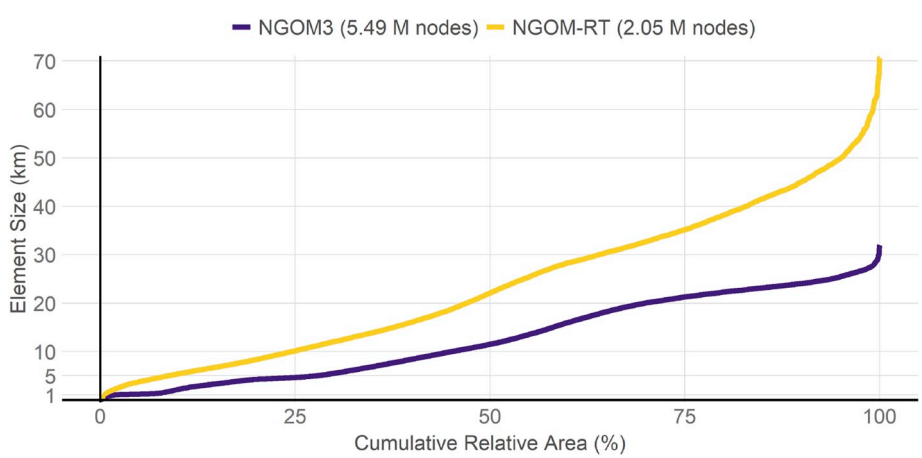

Fig. 9. The local element size (km) related to the cumulative relative area (%) that encompasses the western North Atlantic model domain for the initial NGOM3 and final NGOM-RT unstructured meshes.

Mississippi and southeastern Louisiana and the addition of the flood protection infrastructure in the NGOM-RT model has an effect on the simulated water levels.

4. Benchmarking

4.1. High Performance Computing cluster

The NGOM3 and NGOM-RT ADCIRC + SWAN models were benchmarked on two high-performance computing (HPC) systems, Queenbee2 and Stampede2. These HPC systems were selected as they are employed during a real-time hurricane event with the ADCIRC Prediction System (APS). Model benchmarking was performed in order to determine the reduced computational cost of the NGOM-RT model as well as the expected wall-clock time.

Queenbee2 (http://www.hpc.lsu.edu) is a located in Baton Rouge, Louisiana and is maintained by the Louisiana Optical Network Infrastructure (LONI). It consists of 480 compute nodes of two 10-core 2.8

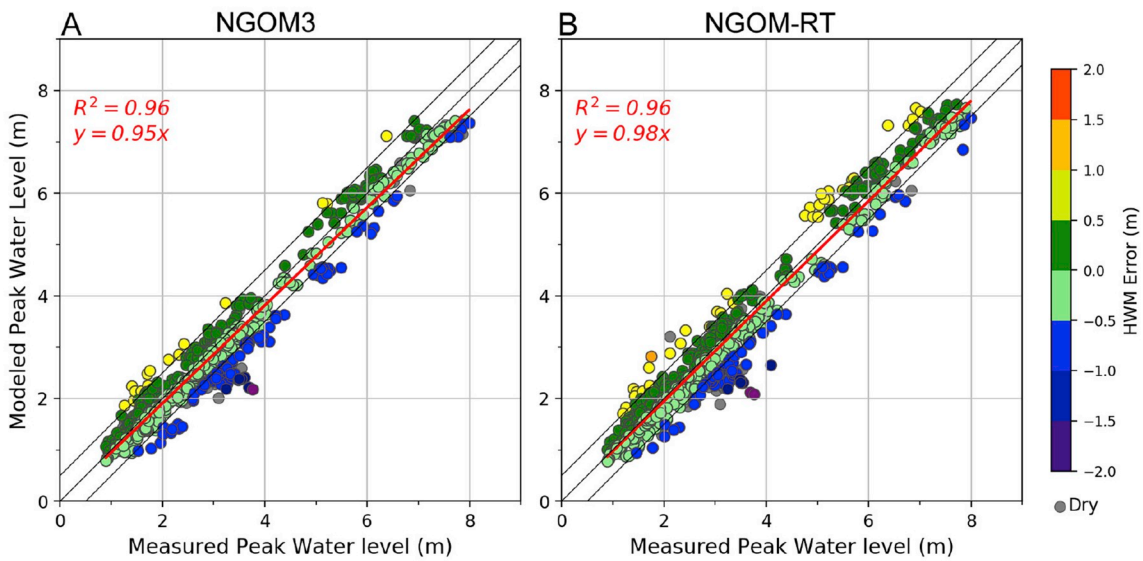

Fig. 10. Comparison of measured and simulated peak surges (high water marks and gage peaks) for Hurricanes Ivan (2004), Dennis (2005), Katrina (2005), and Isaac (2012) for the A) NGOM3 and B) NGOM-RT models.

Table 2
Summary of differences in water level error statistics between the NGOM3 and NGOM-RT model results (NGOM3 - NGOM-RT). SI and bias were only computed for time-series data. Statistics and errors for peak storm surge were only computed if the data set had 10 reliable stations.

Storm	Data Source	No. of stations			ADCIRC to measured HWMs			Estimated ADCIRC errors	
			SI (m)	Bias	No. of HWMs	Slope	R^2	Avg. Abs. Diff. (m)	Std. Dev. (m)
Ivan	NOAA	3	0.01	0.06					
	USACE	8	−0.02	−0.01					
	FEMA				126	−0.01	−0.06	0.02	0.00
	All	11	−0.01	0.01	126	−0.01	−0.06	0.02	0.00
Dennis	NOAA/NDBC	14	−0.01	0.00	14	0.00	−0.01	0.02	0.03
	FEMA				148	0.00	−0.02	0.01	0.01
	All	14	−0.01	0.00	162	−0.01	−0.04	0.01	0.02
Katrina	NOAA	9	−0.02	−0.01					
	USACE	16	−0.01	0.00	12	−0.01	−0.03	−0.02	−0.05
	USGS	7	−0.03	−0.02					
	FEMA				311	−0.02	0.01	−0.01	−0.06
	All	32	−0.02	−0.01	323	−0.02	0.01	−0.01	−0.05
Isaac	NOAA	16	0.08	0.08	16	−0.03	0.01	0.00	0.01
	USGS Perm.	13	0.03	0.05	12	−0.04	0.06	−0.04	−0.10
	USGS SSS	59	0.03	0.00	42	−0.05	0.03	0.04	0.07
	USGS Rapid	7	0.05	0.01					
	NOAA HWM				42	−0.05	0.02	−0.03	−0.07
	All	95	0.04	0.02	112	−0.04	0.01	−0.01	−0.03

GHz E5-2680v2 Xeon processors and 64 GB memory shared across each compute node. The computed nodes are connected via 56 Gb/s FDR Infiniband. The theoretical peak performance of Queenbee2 is 1.5 Petaflops.

Stampede2 (https://portal.tacc.utexas.edu/user-guides/stampede2) is located in Austin, Texas and is maintained by the Texas Advanced Computing Center (TACC). It consists of 4 200 KNL and 1 736 SKX compute nodes. For this study, the SKX compute nodes are exclusively used. The SKX compute nodes contain Intel Xeon Platinum 8 160 ("Skylake") processors with 48 cores on two sockets (24 cores/socket) and nominal clock rate of 2.1 GHz (1.4–3.7 GHz depending on instruction set and number of active cores). Each compute node shares 192 GB of RAM. The compute nodes are connected via a 100 Gb/s Intel Omni-Path network.

4.2. Benchmarking results

The following benchmarking results are presented to connect the reduction in mesh node count to a reduction in wall clock time using the ADCIRC and ADCIRC + SWAN codes. In addition, the results are aimed at highlighting the expected wall clock when running the NGOM3 and NGOM-RT meshes in real-time. The results presented herein are not focused on timing of the ADCIRC and ADCIRC + SWAN codes or to compare speeds of Stampede2 and Queenbee2.

The NGOM3 and NGOM-RT meshes were run with both ADCIRC and ADCIRC + SWAN for Hurricane Katrina. Each run was hot-started at 2005/08/28/0000Z and run for two days until 2005/08/30/0000Z which captures the peak storm surge along the Mississippi coast. This is similar to benchmarking performed by Dietrich et al. (2012) for an ADCIRC + SWAN model of southeastern Louisiana. The generalized asymmetrical Holland vortex model (GAHM) ((Gao, 2018; Cyriac et al., 2018; Dietrich et al., 2018)) was used as the meteorological forcing for all benchmarking simulations - it is the wind model currently used during real-time simulations. Model output was turned off for all runs. The total wall clock for the two-day simulation was normalized to yield wall clock time per day of simulation.

Fig. 11 shows the wall clock time as a function of the total number of compute cores and Fig. 12 shows the wall clock as a function of the

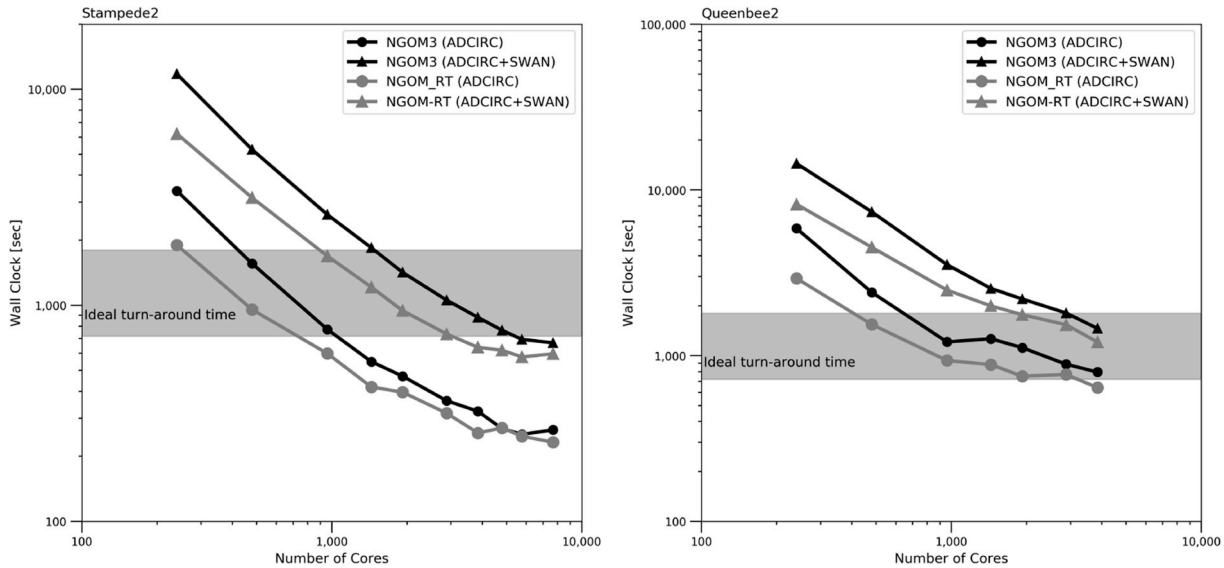

Fig. 11. Wall-clock time (seconds) versus total number of computational cores for the NGOM3 (black) and NGOM-RT (gray) models on Stampede2 (left) and Queenbee2 (right). The shaded region represents the ideal wall clock time to complete a five-day forecast simulation within 1–2 h.

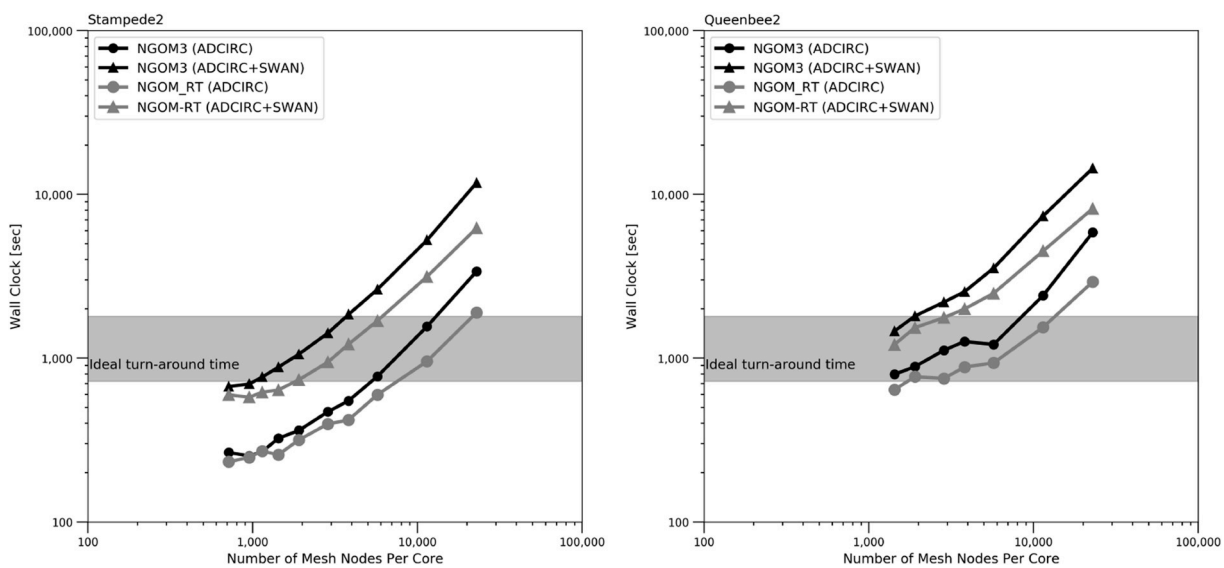

Fig. 12. Wall-clock time (seconds) versus unstructured mesh nodes per core for the NGOM3 (black) and NGOM-RT (gray) models on Stampede2 (left) and Queenbee2 (right). The shaded region represents the ideal wall clock time to complete a five-day forecast simulation within 1–2 h.

number of mesh nodes per core. The black lines represent the timing of the NGOM3 mesh and the gray represents the NGOM-RT mesh. The circle symbols correspond with an ADCIRC only simulation and diamond with an ADCIRC + SWAN simulation. The shaded region in Figs. 11 and 12 represent the ideal wall clock (or turn-around time) of 1–2 h for a five-day forecast simulation.

First, we note that the NGOM3 ADCIRC and ADCIRC + SWAN simulations scale linearly to 5 760 cores on Stampede2. However, the NGOM-RT ADCIRC and ADCIRC + SWAN simulations scale linearly to 3 840 cores. On Queenbee2 the NGOM3 ADCIRC simulations scale until 1 040 cores and ADCIRC + SWAN through 3 840 cores (the maximum number of cores we were able to employ on Queenbee2). The NGOM-RT ADCIRC simulation scales linearly until 1 040 cores and 1 920 cores with ADCIRC + SWAN.

The timing information indicates that the NGOM-RT mesh on Stampede2 can complete a five-day ADCIRC and ADCIRC + SWAN forecast simulation in under 2 h using 240 and 960 cores, respectively, compared to 480 and 1 040 cores with the NGOM3. On Queenbee2, a five-day simulation can complete in less than 2 h using 960 and 1 440 cores on the NGOM-RT mesh using ADCIRC and ADCIRC + SWAN, respectively, and 1 040 and 2 880 cores with the NGOM3 mesh.

Second, we find that the NGOM-RT mesh reaches its scaling limit earlier than NGOM3. The wall clock converges and reaches a lower limit of 270 s at 4 800 cores for the NGOM3 and NGOM-RT ADCIRC simulation on Stampede2. The convergence also corresponds to a lower limit of 1 000 nodes per computational core. The SWAN + ADCIRC simulations on Stampede2 converge at 7 680 cores with a wall clock lower limit of 600 s, which corresponds to a lower limit of 700 mesh nodes per core. The reduced scaling limit of NGOM-RT is a related to the reduced mesh node count. The lower limit of mesh nodes per core is achieved faster with the NGOM-RT mesh. The increased parallel communication becomes the limiting factor when the total number of mesh nodes per computational core is reduced (total number of computational cores is increased).

Furthermore, there is negligible performance decrease in deploying greater than 4 800 and 7 680 Stampede2 cores for an NGOM-RT ADCIRC and ADCIRC + SWAN simulation, respectively. In addition, there is no gain in wall clock time when decomposing the unstructured mesh to less than 1 000 nodes per computational core for an ADCIRC simulation and 700 mesh nodes per core for an ADCIRC + SWAN simulation for either mesh. On Queenbee2 there is a benefit in utilizing up to 3 840 cores and decomposing the mesh into 1 400 nodes per core with NGOM3 and 500 nodes per core with NGOM-RT for both an ADCIRC and ADCIRC + SWAN simulation.

To complete a five-day simulation on Stampede2 in under 2 h the NGOM3 mesh requires a maximum of 10,000 and 4 000 mesh nodes per core for ADCIRC and ADCIRC + SWAN, respectively. The NGOM-RT mesh requires a maximum of 20,000 and 6 000 mesh nodes per core for ADCIRC and ADCIRC + SWAN, respectively. On Queenbee2 an ADCIRC and ADCIRC + SWAN simulation requires a maximum of 9 000 and 2 000 mesh nodes per core, respectively, and 10,000 and 3 000 mesh nodes per on the NGOM-RT mesh.

Finally, we quantify the reduction in wall clock for the NGOM-RT mesh relative to the NGOM3 mesh as shown in Fig. 13. On 240 cores the NGOM-RT mesh is 1.8–2.0 times faster than NGOM3 for ADCIRC and ADCIRC + SWAN on Stampede2 and Queenbee2. On Stampede2, the ADCIRC + SWAN simulation benefits when using larger core counts than ADCIRC only simulations. There is a spike of 1.25 in the normalized speed-up at 3 840 cores on Stampede2 and 1.5 from 1 440–1 920 cores on Queenbee2 for the ADCIRC simulation.

5. Conclusions

Accurate numerical simulation of astronomic tide- and tropical cyclone-driven water level anomalies are dependent on the underlying unstructured mesh and its representation of the natural landscape. Computational hurricane storm surge models are now used to in decision support frameworks during an impending tropical cyclone event to protect lives and property. Therefore, it is imperative that an accurate simulation be performed with a fast turnaround time (1–2 h). In addition, the model must include sufficient detail across the coastal floodplain so guidance can be provided beyond the shoreline where property and infrastructure exist.

Previously developed unstructured mesh generation methods for shallow water equation models, such as LTEA and LTEA + CD, are able to generate computationally efficient unstructured meshes for the deep water and nearshore areas (always wetted). However, there is a gap in such research for computationally efficient mesh generation across the coastal floodplain. This work begins to address this gap while building on previous efforts in order to construct a high-quality unstructured mesh for use in a real-time early-warning hurricane storm surge guidance system.

We utilized a mesh decimation algorithm for the coastal floodplain with the goal of reducing mesh nodes while preserving the representation of the topography. An unstructured mesh was generated via paving scalar density from the obtained size functions along with interior vertical feature constraints and the external model boundary. The resulting mesh, real-time mesh, contains 64% less computational points than the research-grade mesh and preserved the integrity of the meshes representation of the coastal topography. Simulated water levels for both models agree with measurements for Hurricanes Ivan, Dennis, Katrina, and Isaac. Differences in SI and bias for time-series water levels were less than 10 cm and differences in average absolute difference range from −0.04 - 0.02 m. In addition, an ADCIRC + SWAN simulation with the

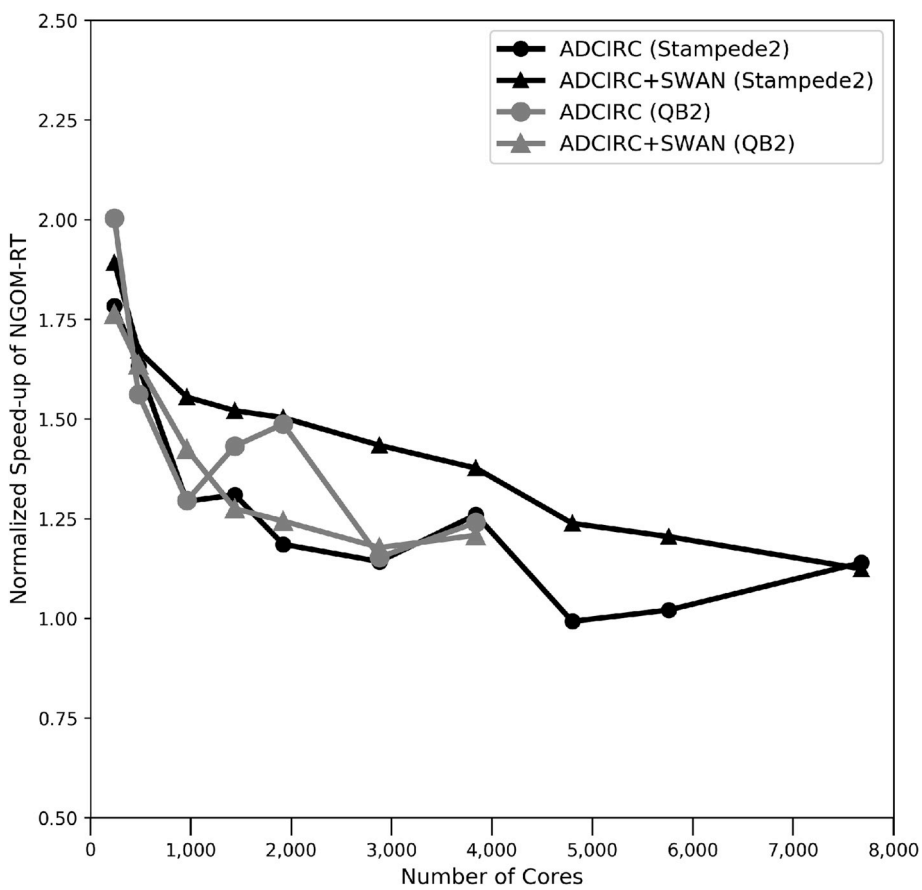

Fig. 13. Normalized speed-up of the NGOM-RT model as a function of total number of cores on Stampede2 (black) and Queenbee2 (gray). The NGOM-RT runs are normalized by the NGOM runs for the same number of cores.

NGOM-RT mesh is 1.5–2.0 times faster than the NGOM3 mesh on up to 1 920 cores on Stampede2 and 960 cores on Queenbee2. The NGOM-RT mesh requires 480 and 960 less cores to perform a five-day ADCIRC + SWAN simulation in under 2 h on Stampede2 and Queenbee2, respectively.

Future work will improve mesh generation across the coastal floodplain with focus on generating computationally efficient meshes. New methods will supplement geometric mesh generation approaches to integrate shallow water hydrodynamics into the mesh generation procedure. The next generation of unstructured mesh generation techniques will be fully-automated and be based on a high-resolution digital elevation models. As computational power continues to increase storm surge forecasting models that provide early warning can increase in their domain size and include higher resolution while continuing to reduce the computational cost.

Acknowledgements

This material is based upon work supported by the U.S. Department of Homeland Security under Grant Award Number 2015-ST-061-ND0001-01. The views and conclusions contained in this document are those of the authors and should not be interpreted as necessarily representing the official policies, either expressed or implied, of the U.S Department of Homeland Security. This research was also funded in part under the National Oceanic and Atmospheric Administration (NOAA) Ecological Effects of Sea Level Rise (EESLR) Program [Award Nos. NA10NOS4780146 and NA16NOS4780208], and the Louisiana Sea Grant Laborde Chair. This work used the Extreme Science and Engineering Discovery Environment (XSEDE), which is supported by the National Science Foundation (NSF) [Award No. ACI-1053575] (Towns et al., 2014). This work also used High Performance Computing at Louisiana State University (LSU) and the Louisiana Optical Network Initiative (LONI). The statements and conclusions are those of the authors and do not necessarily reflect the views of DHS, NOAA, Louisiana Sea Grant, XSEDE, NSF, LSU, or LONI. All data for this paper is properly cited and referred to in the reference list.

Appendix A. Supplementary data

Supplementary data associated with this article can be found, in the online version, at https://doi.org/10.1016/j.coastaleng.2019.103622.

References

Aquaveo, 2014. Surface-water Modeling System.
Ashley, S.T., Ashley, W.S., 2008. Flood fatalities in the United States. Journal of Applied Meteorology and Climatology 47, 805–818.
Atkinson, J., Roberts, H., Hagen, S., Zou, S., Bacopoulos, P., Medeiros, S.C., Weishampel, J., Cobell, Z., 2011. Deriving frictional parameters and performing historical validation for an adcirc storm surge model of the Florida gulf coast. Florida Watershed Journal 4, 22–27.
Bacopoulos, P., Parrish, D., Hagen, S., 2011. Unstructured mesh assessment for tidal model of the south atlantic bight and its estuaries. Journal of Hydraulic Engineering, Special Issue on Coastal Maritime Hydraulics 49, 487–502.
Battjes, J.A., Janssen, J.P.F.M., 1978. Energy loss and set-up due to breaking of random waves. In: Coastal Engineering Proceedings; No 16 (1978): Proceedings of 16th Conference on Coastal Engineering, vol. 1978. Hamburg, Germany.
Becker, J.J., Sandwell, D.T., Smith, W.H.F., Braud, J., Binder, B., Depner, J., Fabre, D., Factor, J., Ingalls, S., Kim, S.H., Ladner, R., Marks, K., Nelson, S., Pharaoh, A., Trimmer, R., Von Rosenberg, J., Wallace, G., Weatherall, P., 2009. Global bathymetry and elevation data at 30 arc seconds resolution: srtm30plus. Mar. Geod. 32, 355–371.
Bilgili, A., Smith, K.W., Lynch, D.R., 2006. Battri: a two-dimensional bathymetry-based unstructured triangular grid generator for finite element circulation modeling. Comput. Geosci. 32, 632–642.
Bilskie, M., Hagen, S.C., 2013. Topographic accuracy assessment of bare earth lidar-derived unstructured meshes. Adv. Water Resour. 52, 165–177.
Bilskie, M., Hagen, S., Medeiros, S.C., Passeri, D., 2014. Dynamics of sea level rise and coastal flooding on a changing landscape. Geophys. Res. Lett. 41, 927–934.
Bilskie, M.V., Coggin, D., Hagen, S.C., Medeiros, S.C., 2015. Terrain-driven unstructured mesh development through semi-automatic vertical feature extraction. Adv. Water Resour. 86 (Part A), 102–118.
Bilskie, M.V., Hagen, S.C., Medeiros, S.C., Cox, A.T., Salisbury, M., Coggin, D., 2016a. Data and numerical analysis of astronomic tides, wind-waves, and hurricane storm surge along the northern gulf of Mexico. J. Geophys. Res.: Oceans 121, 3625–3658.
Bilskie, M.V., Hagen, S.C., Alizad, K., Medeiros, S.C., Passeri, D.L., Needham, H.F., Cox, A., 2016b. Dynamic simulation and numerical analysis of hurricane storm surge under sea level rise with geomorphologic changes along the northern gulf of Mexico. Earth's Future 4, 177–193.
Bilskie, M., Hagen, S., Irish, J.L., 2019. Development of return period stillwater floodplains for the northern gulf of Mexico under the coastal dynamics of sea level rise. J. Waterw. Port, Coast. Ocean Eng. 145, 04018043.
Black, P.G., D'Asaro, E.A., Sanford, T.B., Drennan, W.M., Zhang, J.A., French, J.R., Niiler, P.P., Terrill, E.J., Walsh, E.J., 2007. Air–sea exchange in hurricanes: synthesis of observations from the coupled boundary layer air–sea transfer experiment. Bull. Am. Meteorol. Soc. 88, 357–374.
Booij, N., Ris, R., Holthuijsen, L., 1999. A third-generation wave model for coastal regions 1. model description and validation. J. Geophys. Res. 104, 7649–7666.
Buczkowski, B., Reid, J., Jenkins, J., Reid, C., Williams, S., Flocks, J., 2006. usSEABED: Gulf of Mexico and Caribbean (Puerto Rico and U.S. Virigin Islands) Offshore Surficial Sediment Data Release, Report. U.S. Geological Survey.
Bunya, S., Dietrich, J., Westerink, J., Ebersole, B., Smith, J., Atkinson, J., Jensen, R., Resio, D., Luettich, R., Dawsone, C., Cardone, V., Cox, A., Powell, M., Westerink, H., Roberts, H., 2010. A high-resolution coupled riverine flow, tide, wind, wind wave, and storm surge model for southeastern Louisiana and Mississippi. part i: model development and validation. Mon. Weather Rev. 128.
Burston, J., Ware, D., Tomlinson, R., 2015. The real-time needs of emergency managers for tropical cyclone storm tide forecasting: results of a participatory stakeholder engagement process. Nat. Hazards 78, 1653–1668.
Cavaleri, L., Rizzoli, P., 1981. Wind wave prediction in shallow water: theory and applications. J. Geophys. Res.: Oceans 86, 10961–10973.
Cobell, Z., Zhao, H., Roberts, H.J., Clark, F.R., Zou, S., 2013. Surge and wave modeling for the Louisiana 2012 coastal master plan. J. Coast. Res. 88–108.
Coggin, D., Hagen, S., Salisbury, M.B., 2011. A digital elevation model for franklin, wakulla, and jefferson counties. Florida Watershed Journal 4, 5–10.
Coll, N., Guerrieri, M., Rivara, M.-C., Sellarès, J.A., 2011. Adaptive simplification of huge sets of terrain grid data for geosciences applications. J. Comput. Appl. Math. 236, 1410–1422.
Conroy, C., Kubatko, E., West, D., 2012. Admesh: an advanced, automatic unstructured mesh generator for shallow water models. Ocean Dyn. 62, 1503–1517.
Cox, A., Greenwood, J., Cardone, V., Swail, V., 1995. An Interactive Objective Kinematic Analysis System. Canada, Alberta.
CPRA, 2017. Coastal Master Plan: Model Improvement Plan, Report, vol. 2013. The Water Institute of the Gulf.
Cyriac, R., Dietrich, J.C., Fleming, J.G., Blanton, B.O., Kaiser, C., Dawson, C.N., Luettich, R.A., 2018. Variability in coastal flooding predictions due to forecast errors during hurricane arthur. Coast Eng. 137, 59–78.
Danilov, S., 2013. Ocean modeling on unstructured meshes. Ocean Model. 69, 195–210.
Dietrich, J., Westerink, J., Kennedy, A., Smith, J., Jensen, R., Zijlema, M., Holthuijsen, L., Dawson, C., Luettich, R., Powell, M., Cardone, V., Cox, A., Stone, G., Pourtaheri, H., Hope, M., Tanaka, S., Westerink, L., Westerink, H., Cobell, Z., 2011a. Hurricane gustav (2008) waves and storm surge: hindcast, synoptic analysis, and validation in southern Louisiana. Mon. Weather Rev. 139, 2488–2522.
Dietrich, J., Zijlema, M., Westerink, J., Holthuijsen, L., Dawson, C., Luettich, R., Jensen, R., Smith, J., Stelling, G., Stone, G., 2011b. Modeling hurricane waves and storm surge using integrally-coupled, scalable computations. Coast Eng. 58, 45–65.
Dietrich, J., Tanaka, S., Westerink, J., Dawson, C., Luettich, R., Zijlema, M., Holthuijsen, L., Smith, J., Westerink, L., Westerink, H., 2012. Performance of the unstructured-mesh, swan+adcirc model in computing hurricane waves and surge. J. Sci. Comput. 52, 468–497.
Dietrich, J., Zijlema, M., Allier, P.E., Holthuijsen, L., Booij, N., Meixner, J.D., Proft, J.K., Dawson, C.N., Bender, C.J., Naimaster, A., Smith, J.M., Westerink, J.J., 2013. Limiters for spectral propagation velocities in swan. Ocean Model. 70, 85–102.
Dietrich, J.C., Muhammad, A., Curcic, M., Fathi, A., Dawson, C.N., Chen, S.S., Luettich, R.A., 2018. Sensitivity of Storm Surge Predictions to Atmospheric Forcing during Hurricane Isaac 144, 04017035.
Egbert, G., Erofeeva, S., 2002. Efficient inverse modeling of barotropic ocean tides. J. Atmos. Ocean. Technol. 19, 183–204.
Egbert, G., Bennett, A., Foreman, M., 1994. Topex/poseidon tides estimated using a global inverse model. J. Geophys. Res.: Oceans 99, 24821–24852.
Funakoshi, Y., Hagen, S.C., Bacopoulos, P., 2008. Coupling of hydrodynamic and wave models: case study for hurricane floyd (1999) hindcast. J. Waterw. Port, Coast. Ocean Eng. 134.
Gao, 2018. On the Surface Wind Stress for Storm Surge Modelling. Thesis.
Garland, M., Heckbert, P.S., 1997. Surface simplification using quadric error metrics. In: Proceedings of the 24th Annual Conference on Computer Graphics and Interactive Techniques. ACM Press/Addison-Wesley Publishing Co., pp. 209–216, 258849.
George, P.L., Seveno, E., 1994. The advancing-front mesh generation method revisited. Int. J. Numer. Methods Eng. 37, 3605–3619.
George, P.L., Hecht, F., Saltel, E., 1991. Automatic mesh generator with specified boundary. Comput. Methods Appl. Mech. Eng. 92, 269–288.
Gorman, G.J., Piggott, M.D., Wells, M.R., Pain, C.C., Allison, P.A., 2008. A systematic approach to unstructured mesh generation for ocean modelling using gmt and terreno. Comput. Geosci. 34, 1721–1731.
Hagen, S., 2001. Estimation of the truncation error for the linearized, shallow water momentum equations. Eng. Comput. 17, 354–362.
Hagen, S.C., Parrish, D., 2004. Meshing requirements for tidal modeling in the western north atlantic. Int. J. Comput. Fluid Dyn. 18, 585–595.

Hagen, S.C., Westerink, J.J., Kolar, R.L., 2000. One-dimensional finite element grids based on a localized truncation error analysis. Int. J. Numer. Methods Fluids 32, 241–262.
Hagen, S.C., Westerink, J.J., Kolar, R.L., Horstmann, O., 2001. Two-dimensional, unstructured mesh generation for tidal models. Int. J. Numer. Methods Fluids 35, 669–686.
Hagen, S.C., Horstmann, O., Bennett, R.J., 2002. An unstructured mesh generation algorithm for shallow water modeling. Int. J. Comput. Fluid Dyn. 16, 83–91.
Hagen, S., Zundel, A., Kojima, S., 2006. Automatic, unstructured mesh generation for tidal calculations in a large domain. Int. J. Comput. Fluid Dyn. 20, 593–608.
Hope, M., Westerink, J., Kennedy, A., Kerr, P., Dietrich, J., Dawson, C., Bender, C., Smith, J., Jensen, R., Zijlema, M., Holthuijsen, L., Luettich, R., Powell, M., Cardone, V., Cox, A., Pourtaheri, H., Roberts, H., Atkinson, J., Tanaka, S., Westerink, H., Westerink, L., 2013. Hindcast and validation of Hurricane Ike (2008) waves, forerunner, and storm surge. J. Geophys. Res.: Oceans 118, 4424–4460.
Jia, S., Tang, X., Pan, H., 2006. Fast Mesh Simplification Algorithm Based on Edge Collapse. Springer Berlin Heidelberg, Berlin, Heidelberg, pp. 275–286.
Kennedy, A., Gravois, U., Zachry, B., Westerink, J., Hope, M., Luettich, R., Dean, R.G., 2011. Origin of the hurricane ike forerunner surge. Geophys. Res. Lett. 38.
I. Kinnmark, The Shallow Water Wave Equations: Formulation, Analysis, and Application, Springer-Verlag, New York, New York.
Kolar, R., Gray, W., Westerink, J., Cantekin, M., Blain, C., 1994. Aspects of nonlinear simulations using shallow-water models based on the wave continuity equation. Comput. Fluid 23, 523–538.
Komen, G.J., Hasselmann, K., Hasselmann, K., 1984. On the existence of a fully developed wind-sea spectrum. J. Phys. Oceanogr. 14, 1271–1285.
Luettich, R., Westerink, J., 2004. Formulation and Numerical Implementations of the 2D/3D ADCIRC Finite Element Model Version 44.XX, Report, 12/08/2004.
Luther, M.E., Merz, C.R., Scudder, J., Baig, S.R., Pralgo, J.L.T., Thompson, D., Gill, S., Hovis, G., 2007. Water level observations for storm surge. Mar. Technol. Soc. J. 41, 35–43.
Madsen, O., Poon, Y., Graber, H., 1988. Spectral wave attenuation by bottom friction: Theory. Coastal Engineering Proceedings 492–504.
Martyr, R., Dietrich, J., Westerink, J., Kerr, P., Dawson, C., Smith, J., Pourtaheri, H., Powell, M., Van Ledden, M., Tanaka, S., Roberts, H.J., Westerink, H., Westerink, L., 2013. Simulating hurricane storm surge in the lower Mississippi river under varying flow conditions. J. Hydraul. Eng. 139, 492–501.
Medeiros, S., Hagen, S.C., 2012. Review of wetting and drying algorithms for numerical tidal flow models. Int. J. Numer. Methods Fluids 71, 473–487.
Medeiros, S., Hagen, S., Weishampel, J., 2012. Comparison of floodplain surface roughness parameters derived from land cover data and field measurements. J. Hydrol. 452–453, 139–149.
Medeiros, S., Hagen, S., Weishampel, J., Angelo, J., 2015. Adjusting lidar-derived digital terrain models in coastal marshes based on estimated aboveground biomass density. Remote Sens. 7, 3507.
Morrow, B.H., Lazo, J.K., 2014. Coastal emergency managers' preferences for storm surge forecast communication. J Emerg Manag 12, 153–160.
Munroe, R., Montz, B., Curtis, S., 2018. Getting more out of storm surge forecasts: emergency support personnel needs in North Carolina, Wea. Climate Soc 10, 813–820.
Parrish, D.M., Hagen, S.C., 2007. 2d unstructured mesh generation for oceanic and coastal tidal models from a localized truncation error analysis with complex derivatives. Int. J. Comput. Fluid Dyn. 21, 277–296.
Parrish, D.M., Hagen, S.C., 2009. Incorporating spatially variable bottom stress and coriolis force into 2d, a posteriori, unstructured mesh generation for shallow water models. Int. J. Numer. Methods Fluids 60, 237–261.
Passeri, D., Hagen, S., Bilskie, M., Medeiros, S., 2015a. On the significance of incorporating shoreline changes for evaluating coastal hydrodynamics under sea level rise scenarios. Nat. Hazards 75, 1599–1617.
Passeri, D.L., Hagen, S.C., Medeiros, S.C., Bilskie, M.V., 2015b. Impacts of historic morphology and sea level rise on tidal hydrodynamics in a microtidal estuary (grand bay, Mississippi). Cont. Shelf Res. CSR3698.
Passeri, D.L., Hagen, S.C., Plant, N.G., Bilskie, M.V., Medeiros, S.C., Alizad, K., 2016. Tidal hydrodynamics under future sea level rise and coastal morphology in the northern gulf of Mexico. Earth's Future 4, 159–176.
Persson, P.-O., Strang, G., 2004. A simple mesh generator in matlab. SIAM Rev. 46, 329–345.
Powell, M., 2006. Drag Coefficient Distribution and Wind Speed Dependence in Tropical Cyclones, Report. Atlantic Oceanographic and Meteorological Laboratory.
Powell, M., Houston, S., Amar, L., LMorisseau-Leroy, N., 1998. The hrd real-time hurricane wind analysis system. J. Wind Eng. Ind. Aerodyn. 77–78.
Powell, M.D., Vickery, P.J., Reinhold, T.A., 2003. Reduced drag coefficient for high wind speeds in tropical cyclones. Nature 422, 279–283.
Ris, R., Holthuijsen, L., Booij, N., 1999. A third-generation wave model for coastal regions 2. verification. J. Geophys. Res. 104, 7667–7681.
Roberts, K.J., Pringle, W.J., Westerink, J.J., 2018. Oceanmesh2d 1.0: matlab-based software for two-dimensional unstructured mesh generation in coastal ocean modeling. Geosci. Model Dev. Discuss. (GMDD) 2018, 1–36.
Rogers, W., Hwang, P., Wang, D., 2003. Investigation of wave growth and decay in the swan model: three regional-scale applications*. J. Phys. Oceanogr. 33, 366–389.
Salisbury, M.B., Hagen, S.C., Coggin, D., Bacopoulos, P., Atkinson, J., Roberts, H.J., 2011. Unstructured mesh development for the big bend region (Florida). Florida Watershed Journal 4, 11–14.
Thompson, E., Cardone, V., 1996. Practical modeling of hurricane surface wind fields. J. Waterw. Port, Coast. Ocean Eng. 122, 195–205.
Towns, J., Cockerill, T., Dahan, M., Foster, I., Gaither, K., Grimshaw, A., Hazelwood, V., Lahtrop, S., Lifka, D., Peterson, G., Roskies, F., Scott, J., Wilkins-Diehr, N., 2014. Xsede: accelerating scientific discovery. Comput. Sci. Eng. 16, 62–74.
Westerink, J.J., Luettich JR., R.A., Muccino, J.C., 1994. Modelling tides in the western north atlantic using unstructured graded grids. Tellus 46, 178–199.
Westerink, J., Luettich, R., Feyen, J., Atkinson, J., Dawson, C., Roberts, H., Powell, M., Dunion, J., Kubatko, E., Pourtaheri, H., 2008. A basin- to channel-scale unstructured grid hurricane storm surge model applied to southern lousiana. Mon. Weather Rev. 136, 833–864.
Wolshon, B., Urbina, E., Wilmot, C., Levitan, M., 2005. Review of policies and practices for hurricane evacuation. i: Transportation planning, preparedness, and response 6, 129–142.
Zijlema, M., 2010. Computation of wind-wave spectra in coastal waters with swan on unstructured grids. Coast Eng. 57, 267–277.